Effects of the Skyrme tensor force on 0^+, 2^+, and 3^- states in ^{16}O and ^{40}Ca nuclei within the second random-phase approximation

M. J. Yang,[1] C. L. Bai,[1] H. Sagawa,[2,3] and H. Q. Zhang[4]
[1]*College of Physics, Sichuan University, Chendu 610065, China*
[2]*Center for Mathematics and Physics, University of Aizu, Aizu-Wakamatsu, Fukushima 965-8560, Japan*
[3]*RIKEN, Nishina Center, Wako 351-0198, Japan*
[4]*China Institute of Atomic Energy, Beijing 102413, China*

(Received 9 November 2020; revised 29 January 2021; accepted 13 April 2021; published 14 May 2021)

The effects of the Skyrme tensor force on the natural-parity 0^+, 2^+, and 3^- states in ^{16}O and ^{40}Ca are studied with the subtracted second random-phase approximation (SSRPA) adopting the Skyrme energy density functional. The strength distribution of these normal parity states are calculated with and without tensor interactions. The tensor force produces a small effect on 0^+ and 2^+ states in the random-phase approximation (RPA). However, our study shows that the tensor force has a significant effect on these states due to the coupling between one particle-one hole (1p-1h) and two particle-twp hole (2p-2h) model space in SSRPA; i.e., it increases strength for the low-lying 0^+ and 2^+ states below 10 MeV and shifts the main peak of 2^+ transition downwards by about 1 to 2 MeV. For the negative-parity 3^- state, the tensor force shifts the lowest state downwards obviously, which helps the prediction of experimental data. The effect of the tensor force on the 3^- state is even visible in the 1p-1h RPA model space. We introduce two different parameter sets of tensor forces to clarify the role of the triplet-odd tensor term on the low-lying states. The microscopic structures of the lowest 0^+, 2^+, and 3^- states are examined looking at their 1p-1h and 2p-2h mixing amplitudes.

DOI: 10.1103/PhysRevC.103.054308

I. INTRODUCTION

The low-lying states of nuclei provide important information on nuclear structure. They are associated with the collective excitations, the nuclear deformation, and also the shape coexistence in nuclei. In double-magic nuclei ^{16}O and ^{40}Ca, the low-lying states are of particular interest due to the presence of shapes that coexist at low excitation energy (Refs. [1] and references therein). The low-lying states of the ^{16}O [2–4] and ^{40}Ca [5–9] have been measured in several works. These experimental measurements show the presence of 0^+ states at very low energy, for example, the first 0^+ excited state at 6.05 and 3.35 MeV in ^{16}O and ^{40}Ca, respectively.

These low-lying states were extensively researched by different theoretical models. Microscopically, the shell model [10,11] includes the full model space and provides reasonable results. However, the huge configuration space limits the application of the model for some light nuclei or the ones around the double-magic nuclei. Mean-field models are also applied based on the density functional theory within the 1p-1h model space: the (quasiparticle) random-phase approximation (Q)RPA model [12–15] takes only the (two-quasiparticle) 1p-1h model space into account and provides reasonable results in many nuclei, especially medium-heavy and heavy nuclei. The extended theory of finite Fermi systems includes the single-particle continuum as well as the coupling to low-lying collective states in a consistent microscopic way [16], while the quasiparticle-phonon model includes the coupling between phonons [17]. The particle-vibration-coupling model [18,19] and the particle-phonon-coupling models [20], which take the coupling between single-particle states and phonons into account, improve the description of the low-lying states. The second-order perturbation theory [21] includes the mixing of 2p-2h configurations into 1p-1h ones perturbatively. As more extended models, the second random-phase approximation (SRPA) [22,23] includes self-consistently all the 1p-1h and 2p-2h configurations in the model space to describe the collective excited states of both low-lying and giant resonance states. On the other side, some macroscopic models were also developed such as the phonon damping model [24], hydrodynamical models [25], and the α-cluster model [26].

As a model beyond the 1p-1h RPA model, the SRPA model was formulated many years ago [27,28] and aimed to describe the strength distribution, fine structure, and transition density of nuclear collective excitations in a more realistic way than the RPA model. The pioneering SRPA calculations were done about 40 years ago with diagonal approximation [29–32], which includes the coupling between the 1p-1h and the 2p-2h model space, but did not include the coupling among 2p-2h configurations. In the recent ten years, full SRPA calculations were implemented, and the large-scale SRPA calculations were done in the closed-shell nuclei ^{16}O and ^{40}Ca [22,23,33,34] and for small metallic clusters [35]. The introduction of 2p-2h configurations may cause a double-counting problem [36] and an infrared instability in the SRPA equation [37]. These problems in the SRPA were analyzed and

discussed carefully in Ref. [38]. To ensure the stability of the SRPA equation and overcome the double-counting problem, a subtraction procedure was introduced in the SRPA [39–41], and the method is adopted in this work (subtracted second random-phase approximation, SSRPA). In the SRPA calculations, different nucleon-nucleon interactions were employed, such as the effective interactions, Skyrme [22] and Gogny [42], and a realistic nuclear force Argonne V18 potential [33]. However, the tensor terms have not been included in the previous SRPA or SSRPA calculations.

As an important component of the nucleon-nucleon interaction, the tensor force produces substantial effects on the nuclear ground and collective excited state properties. It is well known that the tensor force plays an important role in explaining the evolution of the magic number in neutron-rich nuclei [43–45], and the effects of the tensor force on various ground state properties were also widely studied in recent years [18,46–57]. In addition, the tensor force produces important effects on the collective excited states [58–85]. In general, the tensor interaction has only a small effect on the ground state in spin-saturated nuclei such as in ^{16}O and ^{40}Ca. However, as reported in the literature, the tensor force has a significant influence on spin-dependent excitations in the RPA model, but produces a minor effect on the spin-independent normal parity excitations [58–60,72].

In this work, we introduce the Skyrme tensor force in the SSRPA for the first time, and specially study the effect of tensor force on the normal-parity collective excited states, including the 2p-2h configuration space. For this purpose, the normal-parity 0^+, 2^+, and 3^- states in the spin-saturated double-closed-shell nuclei ^{16}O and ^{40}Ca are adopted for SSRPA calculations in this paper. The article is organized as follows. In Sec. II the theoretical scheme of the SSRPA and the subtraction method are briefly introduced. Numerical details and convergence procedures are presented in Sec. III. Results with different tensor forces or without tensor force are shown in Sec. IV. Conclusions and perspectives are given in Sec. V.

II. FORMAL SCHEME OF SSRPA

In this section, we briefly display the main formalism of the SSRPA that can be found in several articles (see, for instance, Ref. [41]). In the SRPA model [22,28], the excitation operator $Q_\nu^\dagger$ can be written as follows:

$$Q_\nu^\dagger = \sum_{ph}\left(X_{ph}^\nu a_p^\dagger a_h - Y_{ph}^\nu a_h^\dagger a_p\right) + \sum_{\substack{p_1<p_2\\ h_1<h_2}}\left(X_{p_1p_2h_1h_2}^\nu a_{p_1}^\dagger a_{p_2}^\dagger a_{h_2}a_{h_1}\right.$$
$$\left. - Y_{p_1p_2h_1h_2}^\nu a_{h_1}^\dagger a_{h_2}^\dagger a_{p_2}a_{p_1}\right). \quad (1)$$

The footnotes p, p_1, and p_2 denote particle states, while h, h_1, and h_2 are hole states. X's and Y's are forward and backward amplitudes. The SRPA equation has the same form of RPA equation:

$$\begin{bmatrix} A & B \\ -B^* & -A^* \end{bmatrix}\begin{bmatrix} X^\nu \\ Y^\nu \end{bmatrix} = \hbar\omega_\nu \begin{bmatrix} X^\nu \\ Y^\nu \end{bmatrix}, \quad (2)$$

where

$$A = \begin{pmatrix} A_{11} & A_{12} \\ A_{21} & A_{22} \end{pmatrix}, \quad B = \begin{pmatrix} B_{11} & B_{12} \\ B_{21} & B_{22} \end{pmatrix},$$
$$X = \begin{pmatrix} X_1^\nu \\ X_2^\nu \end{pmatrix}, \quad Y = \begin{pmatrix} Y_1^\nu \\ Y_2^\nu \end{pmatrix}. \quad (3)$$

The indices 1 and 2 are a shorthand notation for the 1p-1h and 2p-2h configurations, respectively. The matrices A_{12} and B_{12} denote the coupling of 1p-1h with 2p-2h configurations, and A_{22} and B_{22} denote the coupling of 2p2h configurations among themselves. The matrix elements of Eq. (3) are equal to

$$\begin{aligned} A_{11} &= A_{ph;p'h'} \\ &= \langle \mathrm{HF}|[a_h^\dagger a_p, [H, a_{p'}^\dagger a_{h'}]]|\mathrm{HF}\rangle \\ &= (E_p - E_h)\delta_{pp'}\delta_{hh'} + \bar{V}_{ph'hp'}, \quad (4) \\ B_{11} &= B_{ph;p'h'} \\ &= -\langle \mathrm{HF}|[a_h^\dagger a_p, [H, a_{h'}^\dagger a_{p'}]]|\mathrm{HF}\rangle \\ &= \bar{V}_{pp'hh'}, \quad (5) \\ A_{12} &= A_{ph;p_1p_2h_1h_2} \\ &= \langle \mathrm{HF}|\left[a_h^\dagger a_p, \left[H, a_{p_1}^\dagger a_{p_2}^\dagger a_{h_2}a_{h_1}\right]\right]|\mathrm{HF}\rangle \\ &= U(h_1h_2)\bar{V}_{p_1p_2ph_2}\delta_{hh_1} - U(p_1p_2)\bar{V}_{hp_2h_1h_2}\delta_{pp_1}, \quad (6) \\ A_{22} &= A_{p_1p_2h_1h_2;p_1'p_2'h_1'h_2'} \\ &= \langle \mathrm{HF}|\left[a_{h_1}^\dagger a_{h_2}^\dagger a_{p_2}a_{p_1}, \left[H, a_{p_1'}^\dagger a_{p_2'}^\dagger a_{h_2'}a_{h_1'}\right]\right]|\mathrm{HF}\rangle \\ &= \left(E_{p_1} + E_{p_2} - E_{h_1} - E_{h_2}\right)U(p_1p_2)U(h_1h_2) \\ &\quad \times \delta_{p_1p_1'}\delta_{p_2p_2'}\delta_{h_1h_1'}\delta_{h_2h_2'} \\ &\quad + U(h_1h_2)\bar{V}_{p_1p_2p_1'p_2'}\delta_{h_1h_1'}\delta_{h_2h_2'} \\ &\quad + U(p_1p_2)\bar{V}_{h_1h_2h_1'h_2'}\delta_{p_1p_1'}\delta_{p_2p_2'} \\ &\quad - U(p_1p_2)U(h_1h_2)U(p_1'p_2')U(h_1'h_2') \\ &\quad \times \bar{V}_{p_1h_1'p_1'h_1}\delta_{p_2p_2'}\delta_{h_2h_2'}, \quad (7) \end{aligned}$$

where E's are the Hartree-Fock (HF) single-particle energies; $U(mn)$ is the antisymmetrizer for the indices m and n, which can be replaced by the exchange operator $[1 - P(mn)]$; and $\bar{V}$ is the residual interaction. Because the quasiboson approximation is used in the derivation, B_{12}, B_{21} and B_{22} are zero.

If the coupling amongst the 2p-2h configuration is neglected, A_{22} will become diagonal, in this approximation A_{22} is calculated by

$$A_{22}^D = \delta_{p_1p_1'}\delta_{p_2p_2'}\delta_{h_1h_1'}\delta_{h_2h_2'}\left(E_{p_1} + E_{p_2} - E_{h_1} - E_{h_2}\right). \quad (8)$$

In the SRPA with the subtraction procedure (SSRPA), A_{11} and B_{11} are modified:

$$A_{11'}^S = A_{11'} + \sum_2 A_{12}(A_{22})^{-1}A_{21'} + \sum_2 B_{12}(A_{22})^{-1}B_{21'},$$
$$B_{11'}^S = B_{11'} + \sum_2 A_{12}(A_{22})^{-1}B_{21'} + \sum_2 B_{12}(A_{22})^{-1}A_{21'}. \quad (9)$$

So A_{22} is used twice in the whole SSRPA calculation, i.e., the first time in the subtraction procedure, Eq. (9), and the second

one in the diagonalizing of the SRPA equation, Eq. (2). In the actual calculation, it is convenient to apply the diagonal approximation in the subtraction procedure so as to simplify the calculation. In this work, the calculations with the full A_{22} are noted by SSRPA$_F$, while the ones with diagonal approximation only in the subtraction procedure are noted by SSRPA$_D$.

III. NUMERICAL DETAILS

In the HF + SSRPA model, we start by solving the HF equations in coordinate space with a radial mesh extending up to 20 fm in a step of 0.1 fm. When the Skyrme HF potential is calculated in the HF program, the single-particle energy and wave functions of the occupied and unoccupied levels can be solved by using the basis expanded with the harmonic oscillator wave functions up to the maximum major quantum number of $N_{\max} = 8$ and 10 for ^{16}O and ^{48}Ca, respectively.

In the next step, the 1p-1h and 2p-2h configurations are chosen according to the selection rule of isospin, parity, and total angular momentum of the transition, together with an energy cutoff. For 1p-1h configurations, the unperturbed transition energy is chosen up to 100 MeV. While for the 2p-2h configurations, the proper energy cutoff for unperturbed configurations that confirms a reasonable convergence in SSRPA calculations should be adopted.

The IS 0^+ strength distribution of ^{16}O calculated with SGII is shown in Fig. 1. In this paper, all the discrete results are smoothed with the Lorentzian function being 1 MeV in width. In Fig. 1(a) the SSRPA$_D$ calculations are performed with 2p-2h energy cutoffs of 60, 70, and 80 MeV. One can find the convergence in the energy region lower than 20 MeV and can find reasonable convergence in higher-energy regions. Figure 1(b) shows the strength distributions obtained by the SSRPA$_D$ and SSRPA$_F$ calculations with an energy cutoff of 60 MeV. It was reported in Ref. [41] that this simplification causes just a small effect. Our calculations also show a consistent result. Therefore, the SSRPA calculation actually denotes the SSRPA$_D$ case

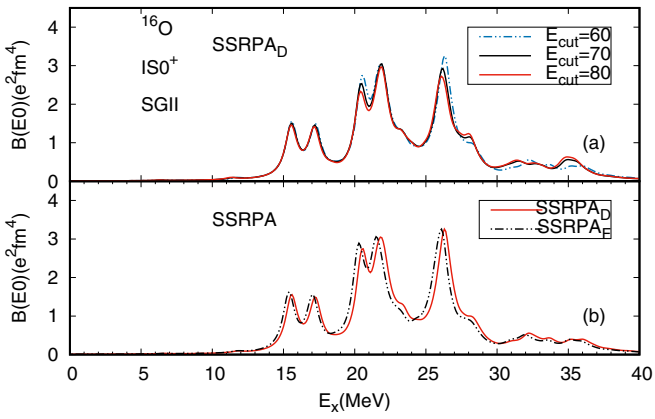

FIG. 1. IS 0^+ strength distributions for ^{16}O calculated by SSRPA$_D$ calculations by the SGII interaction with 2p-2h energy cutoffs of 60, 70, and 80 MeV [panel (a)] and by SSRPA$_D$ and SSRPA$_F$ calculations at $E_{\text{cut}} = 60$ [panel (b)]. See the text for more details.

in this work, and we employ 60 MeV in ^{16}O as the 2p-2h configuration cutoff energy. For ^{40}Ca, the energy cutoff is set at $E_{\text{cut}} = 60$ MeV for 0^+ states and 50 MeV for 2^+ and 3^- states with reasonable convergences in SSRPA calculations.

The transition operators of the spin-independent modes are

$$F_\lambda^{\text{IS}} = \sum_i r_i^n Y_{\lambda 0}(r_i),$$
$$F_\lambda^{\text{IV}} = \sum_i r_i^n Y_{\lambda 0}(r_i)\tau_z(i), \tag{10}$$

in the isoscalar (IS) and isovector (IV) channels, respectively, where $n = \lambda$ except for $\lambda = 0$ with $n = 2$.

After the SRPA equation is diagonalized, the transition strength can be calculated only from the contribution of 1p-1h configurations:

$$B(E_\lambda) = \left|\sum_{ph} b_{ph}(E_\lambda)\right|^2 = \left|\sum_{ph}\left(X_{ph}^\lambda + (-1)^J Y_{ph}^\lambda\right)F_{ph}^\lambda\right|^2. \tag{11}$$

The b_{ph} is the partial contribution to the reduced transition amplitude. The SRPA normalization condition is

$$\sum_{ph}\left(|X_{ph}^\nu|^2 - |Y_{ph}^\nu|^2\right) + \sum_{p_1p_2h_1h_2}\left(|X_{p_1p_2h_1h_2}^\nu|^2 - |Y_{p_1p_2h_1h_2}^\nu|^2\right) = n_1 + n_2 = 1. \tag{12}$$

For 1p-1h and 2p-2h configurations, the contribution of a configuration to the norm of the state A_{1p1h} is

$$A_{1p1h} = |X_{ph}|^2 - |Y_{ph}|^2, \tag{13}$$
$$A_{2p2h} = |X_{p_1p_2h_1h_2}^\nu|^2 - |Y_{p_1p_2h_1h_2}^\nu|^2. \tag{14}$$

And energy moments for the transition are written as

$$m_k = \sum_\nu E_\nu^k B(E_\nu). \tag{15}$$

Table I shows the isoscalar 0^+ and 2^+ energy moments m_1 and m_{-1} obtained by RPA and SSRPA calculations with SGII interaction for ^{16}O and ^{40}Ca calculated. Same as reported in Ref. [41], the m_1 moments are not conserved in the SSRPA calculations compared to the RPA calculations, due to the subtraction procedure, while the m_{-1} moments are conserved by the SSRPA$_F$ calculations, which are almost identical to the RPA ones. The conservation of m_{-1} moments is slightly broken in SSRPA$_D$ calculations by the diagonalization approximation.

In the past decades, much effort has been made to constrain the parameters of the tensor terms, and different strengths of the tensor terms have been adopted to study many physical quantities, such as the single-particle energy [44–46,49,50], the binding energy [53], the spin-isospin transitions [58,72,76], the electromagnetic transitions [59–63], and the β-decay half-life [74,75]. Especially, the role of the Skyrme tensor interactions was discussed extensively in the RPA calculations of Gamow-Teller and spin-dipole states varying the signs and magnitude of tensor terms in the literature [76]. In these works, the triplet-even tensor term is

TABLE I. The energy moments m_1 and m_{-1} of isoscalar 0^+ and 1^+ transitions obtained by the RPA and SSRPA calculations for ^{16}O and ^{40}Ca with SGII interaction.

		^{16}O	
		0^+	
	RPA	SSRPA$_D$	SSRPA$_F$
m_1	673.876	738.777	724.324
m_{-1}	1.169	1.147	1.169
		2^+	
	RPA	SSRPA$_D$	SSRPA$_F$
m_1	8375.433	9831.163	9425.072
m_{-1}	19.471	18.176	19.471
		^{40}Ca	
		0^+	
	RPA	SSRPA$_D$	SSRPA$_F$
m_1	2879.917	3156.741	3091.711
m_{-1}	6.441	6.292	6.441
		2^+	
	RPA	SSRPA$_D$	SSRPA$_F$
m_1	35934.411	39329.832	38566.354
m_{-1}	120.915	116.860	120.915

constrained in a rather narrow range of the strength with the positive sign, but the strength of the triplet-odd term still has a large uncertainty even in the sign. Therefore, in this work, SGII + Te1 and SGII + Te3 [76] are applied to study the effects of different tensor forces, in which the tensor terms were added on the top of SGII [85], with the strengths of the triplet-even and triplet-odd tensor terms T and U set at $(T, U) = (500.0, -350.0)$ and $(650.0, +200.0)$ MeV fm^5, respectively. In the two parameter sets, the strength of the triplet-odd tensor term is in different signs. About the rearrangement term, i.e., the t_3 term, the residual interaction employed in A_{11} and B_{11} is obtained through the derivation of the energy density functional by the density, while in calculations of A_{12} and A_{22} the residual interaction is obtained by the direct antisymmetrization of the t_3 term.

IV. RESULTS AND DISCUSSION

In this section, we present strength distributions of 0^+, 2^+, and 3^- states in ^{16}O and ^{40}Ca. The calculations are done by RPA and SSRPA (actually SSRPA$_D$) models with or without tensor interaction, so as to show the effects of different parameters of tensor force.

A. Strength distributions of 0^+ states

The IS 0^+ strength distributions for ^{16}O calculated by RPA [panel (a)] and SSRPA [panel (b)] with or without tensor force are shown in Fig. 2. Results of different interactions are labeled by SGII (black dashed-dotted lines), SGII + Te1 (red solid lines), and SGII + Te3 (blue dashed-dotted lines), respectively. The effects of the tensor interaction are quite small in RPA calculations; SGII + Te3 produces almost the same results as SGII, and SGII + Te1 shifts the strength downwards within a few KeV. In SSRPA calculations, the effects of tensor

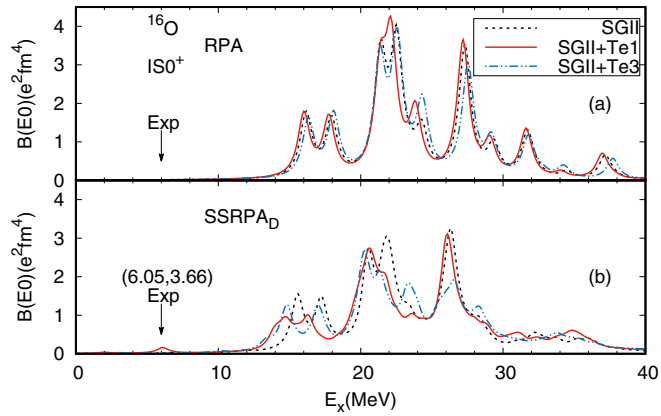

FIG. 2. IS 0^+ strength distributions in ^{16}O. The results are calculated by RPA [panel (a)] and SSRPA [panel (b)] with the interactions SGII (black dashed-dotted lines), SGII + Te1 (red solid lines), and SGII + Te3 (blue dashed-dotted lines). The first observed excited state [3] is represented by an arrow, and the excited energy and the transition strength are shown as E_x and $B(E0)$ in units of MeV and e^2 fm^4, respectively.

force on the strength distribution in the energy region above 20 MeV are notable but not very strong. For SGII + Te3 the strength is expanded to five smaller peaks, and for SGII + Te1 the two peaks around 22 MeV are combined to a peak at about 20.5 MeV. However, in the energy region lower than 20 MeV, the effect of tensor interaction is visible; for SGII + Te3 the two peaks around 18 MeV are shifted downwards by about 1 MeV, while they are shifted downwards further with SGII + Te1. In the energy region lower than 10 MeV, there is no state in the RPA calculations. On the other hand, the first 0^+ excited state appears below 10 MeV and shows better agreement with the experimental energy in the SSRPA calculations without tensor force (as reported in Refs. [22,41]) and also with the tensor terms SGII + Te3. The strength in these calculations is still very weak $B[(E0) \simeq 0.01\ e^2\ \text{fm}^4]$. In the SSRPA calculations with SGII + Te1, the transition strength is larger and visible in Fig. 2(b) at 6.1 MeV with a strength of 0.23 e^2 fm^4. The measured first excited 0^+ state is located at 6.05 MeV, having a much larger strength of 3.66 e^2 fm^4 [3].

The corresponding IV 0^+ strength distributions for ^{16}O are shown in Fig. 3. The tensor force has no appreciable effect on the strength distribution in RPA calculations. In SSRPA models calculated with SGII and SGII + Te3, there are some states but no visible strength distributed in the energy region lower than 10 MeV, while there is visible strength distributed in this energy region with SGII + Te1.

The IS 0^+ strength distributions in ^{40}Ca are shown in Fig. 4. The tensor interaction has a very small impact on the RPA results. Nevertheless, the effect of tensor force on the strength distribution is visible in SSRPA calculations not only in the energy region higher than 10 MeV. At the energy range lower than 10 MeV, there is no state in RPA models. A state with very weak strength appears at the excitation energies 4.91 and 4.81 MeV with strengths of 0.02 and 0.05 e^2 fm^4 in SSRPA models with SGII and SGII + Te3, respectively. In SSRPA models calculated with SGII + Te1, there are two visible peaks at 4.81 and 5.97 MeV with strengths of 0.33 and

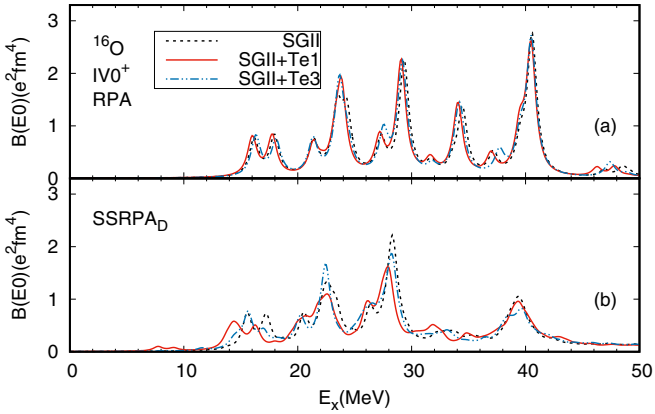

FIG. 3. The same as Fig. 2, but for IV 0^+ strength distributions in ^{16}O.

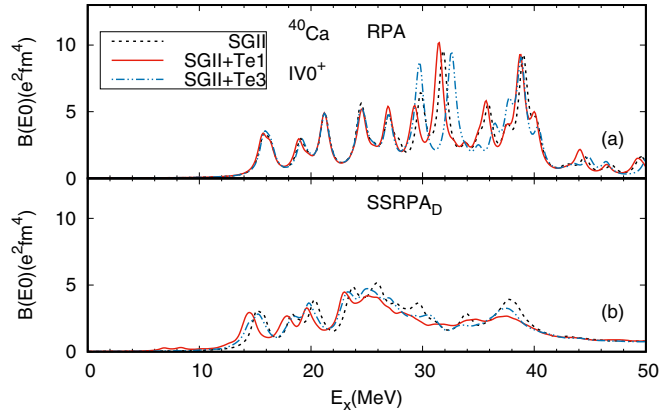

FIG. 5. The same as Fig. 2, but for IV 0^+ in ^{40}Ca.

0.70 e^2 fm^4, while the measured lowest 0^+ state is located at 3.35 MeV with a strength of about 6.4 e^2 fm^4.

The corresponding IV 0^+ strength distributions in ^{40}Ca are shown in Fig. 5. The strength distributions calculated by the RPA with or without tensor force are almost the same at the energy regions blow 28 MeV. In energy region from about 28 to 42 MeV, the strength obtained by SGII + Te1 is slightly shift downwards, but the strength obtained by SGII + Te3 is shifted upwards. In SSRPA calculations, the tensor force in SGII + Te3 shifts the strength downwards, and it shifts the strength further downwards in SGII + Te1. Moreover, in the strength distribution obtained by SGII + Te1, there are two visible states at about 6.8 and 8.3 MeV in Fig. 5, which are not seen in the SSRPA results obtained by SGII or SGII + Te3.

In the two spin-saturated nuclei ^{16}O and ^{40}Ca, the RPA calculations do not produce any state in the energy region lower than 10 MeV, while the SSRPA calculations with SGII or SGII + Te3 can produce some states but the strength is very weak. On the other hand, the SSRPA calculation with SGII + Te1 shifts the strength downwards and produces states with strengths larger than the other SSRPA results in this energy region.

B. Strength distributions of 2^+ states

The IS 2^+ strength distributions in ^{16}O are shown in Fig. 6. As is seen in the figure, there is no state at low energy with or without tensor force in the RPA model, and the tensor force produces no appreciable effect on the IS 2^+ strength distributions. In SSRPA calculations with SGII or SGII + Te3, some states appear at energies lower than 10 MeV with very weak strength, $B(E2) \simeq 0.08$ e^2 fm^4. In SSRPA calculations with SGII + Te1, the main peaks are shifted downwards about 2 MeV, and a state with strength $B(E2) \simeq 0.55$ e^2 fm^4 is found below 10 MeV. The corresponding IV 2^+ strength distributions in ^{16}O are shown in Fig. 7. The effect of tensor force in the RPA is negligible, However the effect of different tensor forces is visible in the SSRPA.

Strength distributions of the IS 2^+ transition in ^{40}Ca are shown in Fig. 8. Similar to the case in ^{16}O, in the RPA model the tensor force has no significant effect on the 2^+ state, the main peak is found at about 16.7 MeV, and no state appears below 10 MeV in calculations with or without including tensor force. In SSRPA calculations with or without tensor force, some states appear below 10 MeV with very weak strength. The summed $B(E2)$ strengths distributed below 10 MeV are

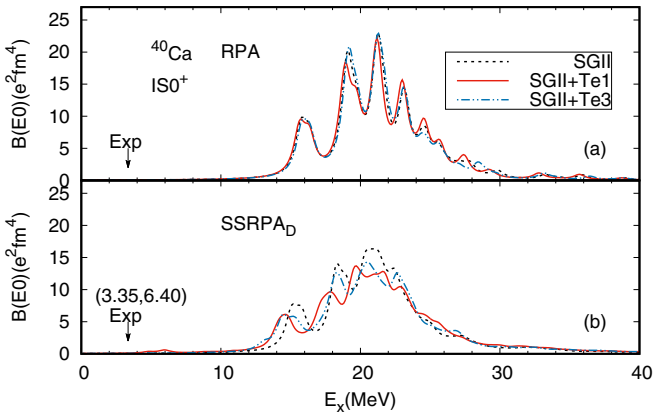

FIG. 4. The same as Fig. 2, but for IS 0^+ in the ^{40}Ca nucleus. The first observed excited state [5] is represented by an arrow, and the excited energy and the transition strength are shown as E_x and $B(E0)$ in units of MeV and e^2 fm^4, respectively.

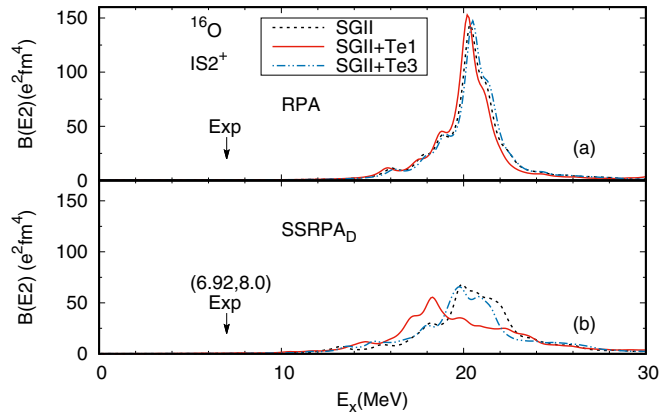

FIG. 6. The same as Fig. 2 but for the IS 2^+ transition in ^{16}O. The first observed excited state [3] is represented by an arrow, and the excited energy and the transition strength are shown as E_x and $B(E2)$ in units of MeV and e^2 fm^4, respectively.

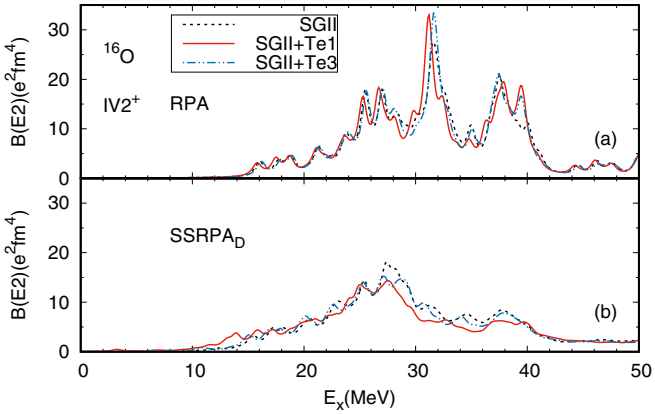

FIG. 7. The same as Fig. 2, but for the IV 2^+ strength distribution in ^{16}O.

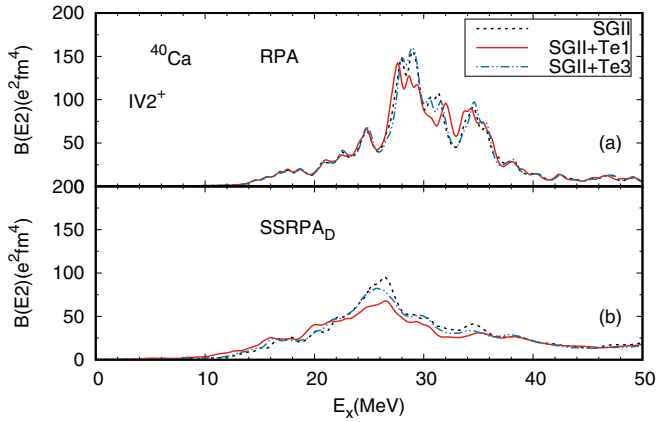

FIG. 9. The same as Fig. 2, but for IV 2^+ in ^{40}Ca.

2.15, 2.15, and 6.96 e^2 fm^4, with SGII, SGII + Te3, and SGII + Te1, respectively. For the main peak, the tensor force shifts the main peak down about 1–2 MeV in the SSRPA calculation with SGII + Te1, while in SGII + Te3 the tensor force has a smaller effect and shifts the main peak upward by about 0.5 MeV.

The corresponding IV 2^+ strength distributions in ^{40}Ca are shown in Fig. 9. The strength is mainly distributed in a wide energy region above 14 MeV, with a main peak at about 28.8 MeV in the RPA. In SSRPA calculations, the strength is expanded in the energy region above 10 MeV. The effect of tensor force reduces the strength in the main peak; the result obtained by SGII gives the strength of the peak about 100 e^2 fm^4, while that obtained by SGII + Te3 is about 80 e^2 fm^4, and the tensor force in SGII + Te1 decreases it further to be about 60 e^2 fm^4.

In short, in RPA calculations with or without tensor force, no state appears in the energy region lower than 10 MeV, while some states appear in this energy region when the SSRPA calculations are done, but the strengths are very weak and invisible as reported in Refs. [22,41]. On the other hand, the present SSRPA calculations with the tensor terms SGII + Te1 increase the transition strengths of the low-energy states below 10 MeV in ^{16}O and ^{40}Ca, but the transition strengths are still weaker than the experimental values. In SSRPA calculations, the tensor force in SGII + Te3 produces very small changes in the IS 2^+ strength distribution in both ^{16}O and ^{40}Ca. However the tensor force SGII + Te1 shifts the main peak downwards by about 1 to 2 MeV, and this effect is strong in the lighter nucleus ^{16}O.

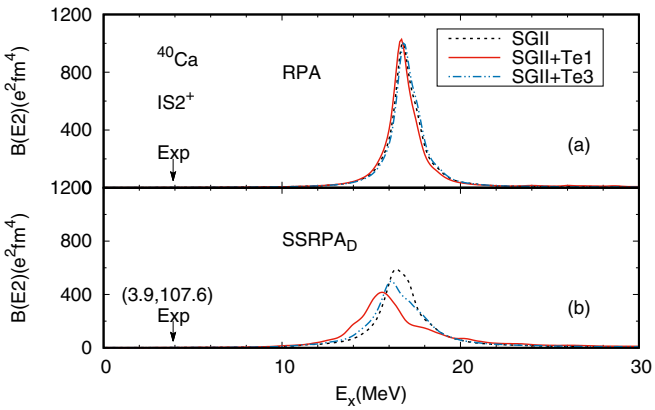

FIG. 8. The same as Fig. 2, but for IS 2^+ in ^{40}Ca. The first observed excited state [9] is represented by an arrow, and the excited energy and the transition strength are shown as E_x and $B(E2)$ in units of MeV and e^2 fm^4, respectively.

C. Strength distribution of 3^- states

In Fig. 10, the IS 3^- strength distributions in ^{16}O by the RPA [panel (a)] and the SSRPA [panel (b)] are shown. The tensor effect on 3^- states is somewhat different from that on the 0^+ and 2^+ states. In RPA calculations, SGII and SGII + Te3 produce almost the same results, while SGII + Te1 produces a very strong effect in the energy region lower than 25 MeV. The lowest peak at about 8 MeV is shifted downwards to about 6 MeV with a $B(E3)$ value of 1441 e^2 fm^6, which reproduces reasonably the experimental one at

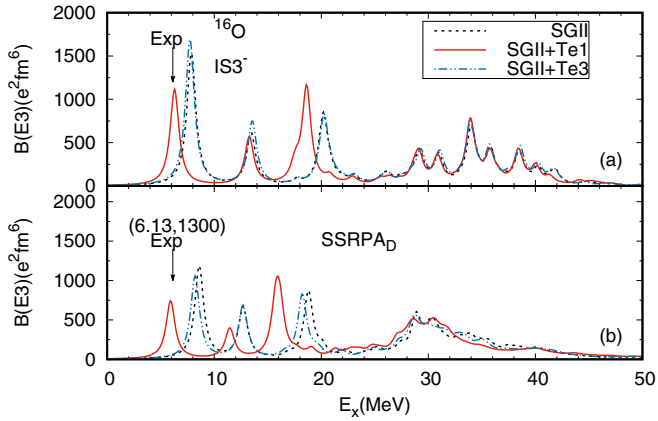

FIG. 10. Isoscalar octupole strength distributions in ^{16}O calculated by RPA [panel (a)] and SSRPA [panel (b)]. Black dashed lines are the SGII results, red solid lines are the SGII + Te1 results, and blue dashed lines are the SGII + Te3 results. Experimental data are taken from Ref. [8] and are shown as E_x and $B(E3)$ in units of MeV and e^2 fm^6, respectively.

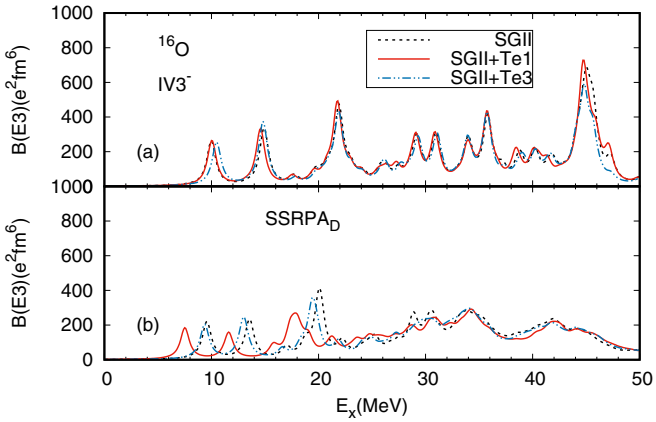

FIG. 11. The same as Fig. 6, but for IV 3^- strength distributions.

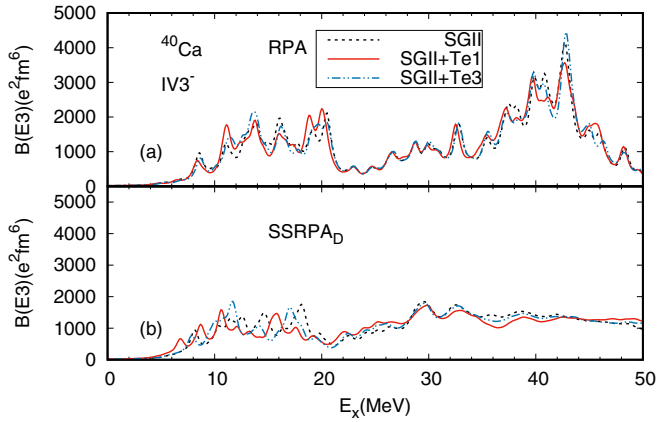

FIG. 13. The same as Fig. 12, but for IV 3^- strength distributions.

about 6.13 MeV with a $B(E3)$ value of 1300 e^2 fm^6. In SSRPA calculations, SGII and SGII + Te3 produce very similar results. In SGII + Te1, the effect of tensor force is visible; it shifts the peak at about 18 MeV to about 16 MeV. Moreover, the low-energy peak is also shifted to about 5.9 MeV with a strength of 1157 e^2 fm^6, which also well reproduces the experimental results.

The IV 3^- strength distributions in ^{16}O calculated by RPA and SSRPA calculations without and with tensor force are shown in Fig. 11. In RPA calculations, the tensor force produces almost no effect on the strength distributions. In SSRPA calculations, the tensor force in SGII + Te1 shifts the strength visibly downwards in the energy region lower than 20 MeV, while SGII + Te3 gives strength distributions almost the same as the one obtained without tensor force.

For the IS 3^- transition in ^{40}Ca, the strength distributions obtained by RPA [panel (a)] and SSRPA [panel (b)] calculations are shown with different tensor forces or without tensor interaction in Fig. 12. In RPA calculations, SGII + Te3 produces almost the same strength distribution as SGII. While in the calculations with SGII + Te1, the low-lying states

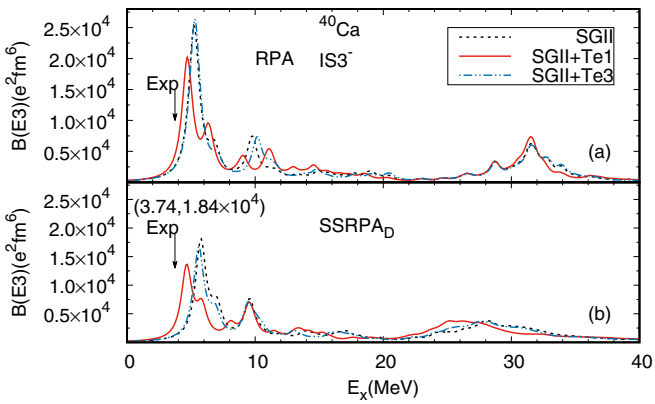

FIG. 12. Strength distributions of IS 3^- in ^{40}Ca calculated by the RPA [panel (a)] and the SSRPA [panel (b)]. Black dashed lines are the SGII results, red solid lines are the SGII + Te1 resulta, and blue dashed lines are the SGII + Te3 results. Experimental data are taken from Ref. [8] and are shown as E_x and $B(E3)$ in units of MeV and 10^3 e^2 fm^6, respectively.

are shifted slightly downwards by the tensor forces to be about 4.7 MeV with a strength of 30.5×10^3 e^2 fm^6, which can be compared with the experimental data at 3.74 MeV with a strength of 18.4×10^3 e^2 fm^6. In SSRPA calculations, SGII + Te3 gives again a negligible effect on the strength distribution. In the calculations with SGII and SGII + Te1, on the other hand, the lowest energy state appears at about 5.6 and 4.6 MeV with strengths of 27×10^3 and 19.9×10^3 e^2 fm^6, respectively. It is noticed that the tensor effect with SGII + Te1 improves significantly the results in comparison with the SGII results and reproduces well the experimental data.

The IV 3^- strength distributions in ^{40}Ca are shown in Fig. 13. The strengths are distributed in a very wide energy region higher than 8 MeV. The effect of tensor force is not visible in both RPA and SSRPA models in the energy region higher than 20 MeV. For the energy region lower than 20 MeV, the tensor force in SGII + Te1 slightly expands the strength distributions to a wider energy region, and some strengths are shifted down in the energy region around 6 MeV.

For 3^- states in both ^{16} and ^{40}Ca, SGII + Te3 and SGII produce almost the same results. However, SGII + Te1 shifts the IS strength downwards visibly, particularly for the low-energy state, which helps to reproduce the experimental results not only of the excitation energy but also of the strength. Moreover, comparing the strength distributions obtained by SSRPA and RPA calculations, the tensor force works significantly on the low-energy IS 3^- peak, even in the 1p-1h configurations in the RPA.

D. Microscopic structure of the low-lying states

In Sec. IV. we discussed the effects of the different tensor force added on the top of SGII, and the tensor force in SGII + Te1 has visible effects on low-lying states. It will be useful to study the 2p-2h configurations and their amplitudes to understand why the $B(E0)$ and $B(E2)$ values of the first excited states are not comparable with the experimental ones, but $B(E3)$ is comparable. The amplitudes provide also the information on why the effect of the tensor force is different on the strength of the first 0^+, 2^+, and 3^+ excited states. In the RPA and the SSRPA, the collectivity might be indicated

TABLE II. The major 1p-1h and 2p-2h configurations of the lowest 0^+ excited states in ^{16}O at 6.10 MeV obtained by SSRPA$_D$ calculations with SGII + Te1. The superscripts π and ν refer to proton and neutron states, respectively. The norms of the 1p-1h configuration A_{1p1h} and the 2p-2h configuration A_{2p2h} are defined in Eqs. (13) and (14). 2p-2h configurations are written as $[(h_1p_1)^{J_1}_{\pi/\nu}(h_2p_2)^{J_2}_{\pi/\nu}]^J$. In the last three columns, the numbers and the sum of the corresponding A_{2p2h} amplitudes are listed in three different ranges of the magnitudes.

1p-1h conf.	A_{1p1h}
$(1s_{1/2}, 2s_{1/2})^\pi$	0.012
$(1p_{3/2}, 3p_{3/2})^\pi$	0.0013
$(1p_{3/2}, 4p_{3/2})^\pi$	0.0013
$(1p_{1/2}, 2p_{1/2})^\pi$	0.0033
$(1p_{1/2}, 3p_{1/2})^\pi$	0.0047
$(1p_{1/2}, 4p_{1/2})^\pi$	0.0029
$(1s_{1/2}, 2s_{1/2})^\nu$	0.012
$(1p_{3/2}, 3p_{3/2})^\nu$	0.0012
$(1p_{3/2}, 4p_{3/2})^\nu$	0.0012
$(1p_{1/2}, 2p_{1/2})^\nu$	0.0033
$(1p_{1/2}, 3p_{1/2})^\nu$	0.0046
$(1p_{1/2}, 4p_{1/2})^\nu$	0.0027
2p-2h conf.	A_{2p2h}
$[(1p_{3/2}, 2s_{1/2})^1_\pi(1p_{1/2}, 1d_{3/2})^1_\pi]^0$	0.0157
$[(1p_{3/2}, 2s_{1/2})^2_\pi(1p_{1/2}, 1d_{3/2})^2_\pi]^0$	0.1397
$[(1p_{3/2}, 2s_{1/2})^2_\pi(1p_{1/2}, 2d_{3/2})^2_\pi]^0$	0.0221
$[(1p_{3/2}, 2s_{1/2})^2_\pi(1p_{1/2}, 3d_{3/2})^2_\pi]^0$	0.0113
$[(1p_{3/2}, 2s_{1/2})^2_\pi(1p_{1/2}, 1d_{3/2})^2_\nu]^0$	0.0591
$[(1p_{3/2}, 1d_{3/2})^0_\pi(1p_{1/2}, 2s_{1/2})^0_\nu]^0$	0.0222
$[(1p_{1/2}, 2s_{1/2})^0_\pi(1p_{3/2}, 1d_{3/2})^0_\nu]^0$	0.0223
$[(1p_{1/2}, 1d_{3/2})^2_\pi(1p_{3/2}, 2s_{1/2})^2_\nu]^0$	0.0517
$[(1p_{1/2}, 2s_{1/2})^0_\pi(1p_{1/2}, 2s_{1/2})^0_\nu]^0$	0.0456
$[(1p_{1/2}, 2s_{1/2})^1_\pi(1p_{1/2}, 2s_{1/2})^1_\nu]^0$	0.0249
$[(1p_{1/2}, 1d_{3/2})^2_\pi(1p_{1/2}, 1d_{3/2})^2_\nu]^0$	0.0196
$[(1p_{3/2}, 2s_{1/2})^1_\nu(1p_{1/2}, 1d_{3/2})^1_\nu]^0$	0.0168
$[(1p_{3/2}, 2s_{1/2})^2_\nu(1p_{1/2}, 1d_{3/2})^2_\nu]^0$	0.1501
$[(1p_{3/2}, 2s_{1/2})^2_\nu(1p_{1/2}, 2d_{3/2})^2_\nu]^0$	0.0135
Number of conf. ($\sum A_{2p2h}$)	Range of A_{2p2h}
225(0.0726)	0.0001–0.001
84(0.2403)	0.001–0.01
14(0.6150)	$\geqslant$0.01

by how many 1p-1h configurations contribute to enhance the transition strength. In this section, the microscopic structure of the low-lying 0^+, 2^+, and 3^- states obtained by SSRPA calculations with SGII + Te1 is studied by looking at the norm of amplitudes A_{1p1h} and A_{2p2h} in Eqs. (13) and (14).

Main 1p-1h configurations and 2p-2h configurations of the lowest 0^+ states in ^{16}O are tabulated in Table II for states at 6.10 MeV. For each state, the configurations with $A_{1p1h} \geqslant 0.001$ are listed in Table II. Because the number of 2p-2h configurations is large, only the configurations with $A_{2p2h} \geqslant 0.01$ are listed. The numbers of the 2p-2h configurations in the three different magnitude ranges of A_{2p2h} amplitudes and the corresponding sum of A_{2p2h} amplitudes are also listed in the last three lines of Table II. There are 12 1p-1h configurations and 98 2p-2h configurations that make important contributions in Table II. The sum of the A_{2p2h} amplitudes of these 98 2p-2h configurations is about 0.92, which explains why the strength obtained by the SSRPA is small compared with the

TABLE III. The same as Table. II but for 2^+_1 states in ^{16}O. The states are located at 5.78 MeV and obtained by the SSRPA with Te1 tensor force.

2p-2h conf.	A_{2p2h}
$[(1p_{3/2}, 2s_{1/2})^2_\pi(1p_{1/2}, 1d_{5/2})^3_\pi]^2$	0.0187
$[(1p_{3/2}, 1d_{5/2})^4_\pi(1p_{3/2}, 1d_{5/2})^4_\nu]^2$	0.0185
$[(1p_{3/2}, 2s_{1/2})^2_\pi(1p_{1/2}, 1d_{5/2})^3_\nu]^2$	0.0132
$[(1p_{3/2}, 1d_{5/2})^2_\pi(1p_{1/2}, 2s_{1/2})^0_\nu]^2$	0.0291
$[(1p_{3/2}, 1d_{5/2})^2_\pi(1p_{1/2}, 1d_{5/2})^2_\nu]^2$	0.0128
$[(1p_{3/2}, 1d_{5/2})^3_\pi(1p_{1/2}, 1d_{5/2})^3_\nu]^2$	0.0118
$[(1p_{3/2}, 1d_{5/2})^4_\pi(1p_{1/2}, 1d_{5/2})^2_\nu]^2$	0.0102
$[(1p_{1/2}, 1d_{5/2})^3_\pi(1p_{1/2}, 1d_{5/2})^3_\pi]^2$	0.0102
$[(1p_{1/2}, 1d_{5/2})^2_\pi(1p_{3/2}, 1d_{5/2})^2_\nu]^2$	0.0262
$[(1p_{1/2}, 1d_{5/2})^2_\pi(1p_{3/2}, 1d_{5/2})^4_\nu]^2$	0.0109
$[(1p_{1/2}, 1d_{5/2})^3_\pi(1p_{3/2}, 1d_{5/2})^4_\nu]^2$	0.0104
$[(1p_{1/2}, 2s_{1/2})^0_\pi(1p_{1/2}, 1d_{5/2})^2_\nu]^2$	0.0338
$[(1p_{1/2}, 2s_{1/2})^1_\pi(1p_{1/2}, 1d_{5/2})^2_\nu]^2$	0.0115
$[(1p_{1/2}, 1d_{5/2})^2_\pi(1p_{1/2}, 2s_{1/2})^0_\nu]^2$	0.0165
$[(1p_{1/2}, 1d_{5/2})^2_\pi(1p_{1/2}, 1d_{5/2})^2_\nu]^2$	0.3312
$[(1p_{1/2}, 1d_{5/2})^3_\pi(1p_{1/2}, 1d_{5/2})^3_\nu]^2$	0.0896
$[(1p_{1/2}, 1d_{5/2})^2_\pi(1p_{1/2}, 1d_{5/2})^1_\nu]^2$	0.0145
Number of conf. ($\sum A_{2p2h}$)	Range of A_{2p2h}
234(0.0741)	0.0001–0.001
71(0.2177)	0.001–0.01
17(0.6696)	$\geqslant$0.01

TABLE IV. The major 1p-1h configurations and 2p-2h configurations of the lowest 3^-_1 states in ^{16}O. The state located at 5.9 MeV is obtained by SSRPA calculations with Te1 tensor force.

1p-1h conf.	A_{1p1h}
$(1p_{3/2}, 1d_{5/2})^\pi$	0.004
$(1p_{1/2}, 1d_{5/2})^\pi$	0.361
$(1p_{3/2}, 1d_{5/2})^\nu$	0.004
$(1p_{1/2}, 1d_{5/2})^\nu$	0.347
2p-2h conf.	A_{2p2h}
$[(1s_{1/2}, 2s_{1/2})^1_\pi(1p_{1/2}, 1d_{5/2})^2_\pi]^3$	0.0148
$[(1s_{1/2}, 2s_{1/2})^1_\nu(1p_{1/2}, 1d_{5/2})^2_\nu]^3$	0.0161
Number of conf. ($\sum A_{2p2h}$)	Range of A_{2p2h}
405(0.1207)	0.0001–0.001
37(0.0904)	0.001–0.01
2(0.0309)	$\geqslant$0.01

TABLE V. The same as Table II, but for the lowest 0_1^+ states in ^{40}Ca. The state located at 4.8 MeV is obtained by SSRPA calculations with Te1 tensor force.

1p-1h conf.	A_{1p1h}
$(1p_{3/2}, 2p_{3/2})^{\pi}$	0.0011
$(1p_{1/2}, 2p_{1/2})^{\pi}$	0.0028
$(1d_{3/2}, 2d_{3/2})^{\pi}$	0.0013
$(1d_{3/2}, 3d_{3/2})^{\pi}$	0.0031
$(1d_{3/2}, 4d_{3/2})^{\pi}$	0.0018
$(1d_{3/2}, 5d_{3/2})^{\pi}$	0.0006
$(1p_{3/2}, 2p_{3/2})^{\nu}$	0.0017
$(1p_{1/2}, 2p_{1/2})^{\nu}$	0.0039
$(1d_{3/2}, 2d_{3/2})^{\nu}$	0.0022
$(1d_{3/2}, 3d_{3/2})^{\nu}$	0.0038
$(1d_{3/2}, 4d_{3/2})^{\nu}$	0.0019
$(1d_{3/2}, 5d_{3/2})^{\nu}$	0.0008
2p-2h conf.	A_{2p2h}
$[(1d_{5/2}, 2p_{3/2})^4_{\pi}(1d_{3/2}, 1f_{5/2})^4_{\pi}]^0$	0.0126
$[(2s_{1/2}, 2p_{3/2})^1_{\pi}(1d_{3/2}, 2p_{1/2})^1_{\pi}]^0$	0.0119
$[(2s_{1/2}, 2p_{3/2})^2_{\pi}(1d_{3/2}, 2p_{1/2})^2_{\pi}]^0$	0.0670
$[(2s_{1/2}, 2p_{3/2})^2_{\pi}(1d_{3/2}, 2p_{1/2})^2_{\nu}]^0$	0.0161
$[(2s_{1/2}, 2p_{3/2})^2_{\pi}(1d_{3/2}, 1f_{7/2})^2_{\nu}]^0$	0.0115
$[(2s_{1/2}, 2p_{1/2})^0_{\pi}(1d_{3/2}, 1p_{3/2})^0_{\nu}]^0$	0.0394
$[(1d_{3/2}, 2p_{3/2})^0_{\pi}(1d_{3/2}, 2p_{3/2})^0_{\pi}]^0$	0.0111
$[(1d_{3/2}, 2p_{3/2})^2_{\pi}(1d_{3/2}, 2p_{3/2})^2_{\pi}]^0$	0.0124
$[(1d_{3/2}, 2p_{3/2})^0_{\pi}(2s_{1/2}, 2p_{1/2})^0_{\nu}]^0$	0.0385
$[(1d_{3/2}, 2p_{1/2})^2_{\pi}(2s_{1/2}, 2p_{3/2})^2_{\nu}]^0$	0.0154
$[(1d_{3/2}, 1f_{7/2})^2_{\pi}(2s_{1/2}, 2p_{3/2})^2_{\nu}]^0$	0.0101
$[(1d_{3/2}, 2p_{3/2})^0_{\pi}(1d_{3/2}, 2p_{3/2})^0_{\nu}]^0$	0.0602
$[(1d_{5/2}, 2p_{3/2})^4_{\nu}(1d_{3/2}, 1f_{5/2})^4_{\nu}]^0$	0.0181
$[(2s_{1/2}, 2p_{3/2})^1_{\nu}(1d_{3/2}, 2p_{1/2})^1_{\nu}]^0$	0.0202
$[(2s_{1/2}, 2p_{3/2})^2_{\nu}(1d_{3/2}, 2p_{1/2})^2_{\nu}]^0$	0.1082
$[(2s_{1/2}, 1f_{7/2})^4_{\nu}(1d_{3/2}, 1f_{5/2})^4_{\nu}]^0$	0.0101
$[(1d_{3/2}, 2p_{3/2})^0_{\nu}(1d_{3/2}, 2p_{3/2})^0_{\nu}]^0$	0.0157
$[(1d_{3/2}, 2p_{3/2})^2_{\nu}(1d_{3/2}, 2p_{3/2})^2_{\nu}]^0$	0.0173
Number of conf. ($\sum A_{2p2h}$)	Range of A_{2p2h}
407(0.1158)	0.0001–0.001
106(0.3106)	0.001–0.01
18(0.4960)	$\geqslant$0.01

experimental one because these 2p-2h states do not make any transition strength.

In Table III, the main configurations for the 2_1^+ state in ^{16}O are listed. There is no 1p-1h configuration that has a norm larger than 0.001, which suggests a weak $B(E2)$ value for the 2_1^+ state in SSRPA. However, there are 17 2p-2h configurations with A_{2p2} larger than 0.01, which may hint that this state is produced mainly by 2p-2h transitions.

The large norms of the excited 0_1^+ state in ^{16}O are found between two major shell 1p-1h excitations $(1s_{1/2}, 2s_{1/2})^{\pi,\nu}$ in Table II for SSRPA, and for this configuration the tensor force has no effect in the RPA model because of the angular momentum selection. For the 2_1^+ state, the largest norms are 0.004, which are found in the $(1s_{1/2}, 1d_{5/2})^{\pi,\nu}$ non-spin-flip excitations. The tensor force in general has a small effect on the non-spin-flip excitation because of its tensor nature of spin-spin coupling. This is the reason why the tensor force has only negligible effect on 0^+ and 2^+ states in the RPA level.

TABLE VI. The same as Table III but for 2_1^+ states in ^{40}Ca. The states located at 3.66 MeV, obtained by SSRPA calculations with Te1 tensor force. There is no 1p-1h state with $A_{1p1h} > 0.001$.

2p-2h conf.	A_{2p2h}
$[(1d_{3/2}, 1f_{7/2})^2_{\pi}(1d_{3/2}, 1f_{7/2})^2_{\pi}]^2$	0.0108
$[(1d_{3/2}, 1f_{7/2})^5_{\pi}(1d_{3/2}, 1f_{7/2})^5_{\pi}]^2$	0.0114
$[(1d_{3/2}, 1f_{7/2})^2_{\pi}(1d_{3/2}, 1f_{7/2})^2_{\nu}]^2$	0.3932
$[(1d_{3/2}, 1f_{7/2})^2_{\pi}(1d_{3/2}, 1f_{7/2})^3_{\nu}]^2$	0.0405
$[(1d_{3/2}, 1f_{7/2})^2_{\pi}(1d_{3/2}, 1f_{7/2})^4_{\nu}]^2$	0.0130
$[(1d_{3/2}, 1f_{7/2})^3_{\pi}(1d_{3/2}, 1f_{7/2})^2_{\nu}]^2$	0.0418
$[(1d_{3/2}, 1f_{7/2})^4_{\pi}(1d_{3/2}, 1f_{7/2})^2_{\nu}]^2$	0.0139
$[(1d_{3/2}, 1f_{7/2})^5_{\pi}(1d_{3/2}, 1f_{7/2})^5_{\nu}]^2$	0.2080
$[(1d_{3/2}, 1f_{7/2})^5_{\nu}(1d_{3/2}, 1f_{7/2})^5_{\nu}]^2$	0.0104
Number of conf. ($\sum A_{2p2h}$)	Range of A_{2p2h}
202(0.0586)	0.0001–0.001
56(0.1609)	0.001–0.01
9(0.7432)	$\geqslant$0.01

The norms for the 3_1^- state in ^{16}O, tabulated in Table IV, show two major p-h configurations, spin-flip $(1p_{1/2}, 1d_{5/2})^{\pi,\nu}$ excitations with additional configurations $(1p_{3/2}, 1d_{5/2})^{\pi,\nu}$. The configurations $(1p_{1/2}, 1d_{5/2})^{\pi,\nu}$ are spin-flip one major shell p-h excitations and the tensor force has an appreciable effect on these spin-flip p-h states. Moreover, as shown in Table IV, the sum of the norms for the important 1p-1h is about 0.7, which suggests the important effect of tensor force in the transition amplitudes through 1p-1h correlations.

In Tables V, VI, and VII, the calculated norms of 0_1^+, 2_1^+, and 3_1^- states in ^{40}Ca are tabulated. The characteristic features

TABLE VII. The major 1p-1h configurations and 2p-2h configurations for the low-lying 3^- states in ^{40}Ca. The state located at 4.65 MeV is obtained by SSRPA calculations with Te1 tensor force. There is no 2p-2h state with $A_{2p2h} > 0.01$.

1p-1h conf.	A_{1p1h}
$(1d_{5/2}, 1f_{7/2})^{\pi}$	0.011
$(2s_{1/2}, 1f_{7/2})^{\pi}$	0.094
$(1d_{3/2}, 1f_{7/2})^{\pi}$	0.301
$(1d_{5/2}, 1f_{7/2})^{\nu}$	0.011
$(2s_{1/2}, 1f_{7/2})^{\nu}$	0.082
$(1d_{3/2}, 1f_{7/2})^{\nu}$	0.243
Number of conf. ($\sum A_{2p2h}$)	Range of A_{2p2h}
398(0.1057)	0.0001–0.001
19(0.0267)	0.001–0.01
0(0)	$\geqslant$0.01

of A_{ph} for these states in ^{40}Ca are similar to those of ^{16}O. The 1p-1h amplitudes of 0_1^+ and 2_1^+ states are rather small so that the transition strengths are much weaker than the experimental data. The main 1p-1h configurations of the 3_1^- state in Table VII on the other hand are large and give the strong $B(E3)$ value, which is comparable with the experimental data. The spin-flip $(1d_{3/2}, 1f_{7/2})^{\pi,\nu}$ configurations are dominated in the A_{1p1h} amplitudes associated with $(1d_{5/2}, 1f_{7/2})^{\pi,\nu}$ and $(2s_{1/2}, 1f_{7/2})^{\pi,\nu}$ configurations. The spin-flip configurations are sensitive to the tensor force even in the RPA level and induce a substantial effect in Fig. 12. There are no 2p-2h configurations with $A_{2p2h} \geqslant 0.01$ in the case of the 3_1^- state.

V. CONCLUSIONS

In this work, we have performed RPA and SSRPA calculations with Skyrme tensor force for describing IS and IV 0^+, 2^+, and 3^- excited states in ^{16}O and ^{40}Ca. To avoid the double counting and divergence in SRPA, the subtracting procedure was adopted in the SSRPA calculations. An advantage of the subtraction procedure is that the SSRPA calculation converges quickly with respect to the energy cutoff.

As stated in Sec. III, the strength of the tensor terms is not well constrained, and there are even uncertainties on the sign of the triplet-odd tensor term. In the calculations, two different tensor parametrizations, SGII + Te1 and SGII + Te3, have been adopted, in which the strengths of the triplet-odd tensor term are in different signs and set at $U = -350.0$ and $+200.0$ MeV fm^5, respectively.

The present study shows that the tensor force in SGII + Te1 has important effects on the coupling between 1p-1h and 2p-2h model spaces. For the IS 0^+ transitions in ^{16}O and ^{40}Ca, in SSRPA calculations the tensor force plays an important role in increasing the strength of the low-lying states below 10 MeV and make them visible in the scale of the present figures. For the IS 2^+ state, the tensor force produces negligible effects in RPA calculations, while in SSRPA calculations the tensor force shifts the main peak by about 1 to 2 MeV; in addition the tensor force also increases the strength in the energy region below 10 MeV, but the peaks are still invisible. For the negative-parity 3^- state, the tensor force shifts visibly the lowest peak downwards by about 2 to 3 MeV in ^{16}O and 1 to 1.5 MeV in ^{40}Ca, so as to make substantial improvements for the predictions of the lowest 3_1^- states in both excitation energies and transition strengths. This effect manifests itself even in the 1p-1h RPA correlation level.

We can see in the SSRPA calculations a clear difference between the effect of two tensor interactions in SGII + Te1 and SGII + Te3, in which the triplet-odd tensor term varies from -350.0 to 200.0 MeV fm^5. The effects of triplet-even and triplet-odd tensor forces of SGII + Te3 on the 0^+, 2^+, and 3^+ states cancel each other and do not give any substantial effect. On the other hand, in the SGII + Te1 case, two tensor terms are added up and give the important effect to improve the numerical results. These results suggest the importance of the triplet-odd term for the realistic calculations of collective states as well as the triplet-even term.

It should be noted that many tensor parameter sets are available in the literature with many combinations of signs and magnitudes for α_T and β_T, as was presented in Ref. [48]. With the four combinations of signs for α_T and β_T and different strengths of these parameters, one can anticipate that the influence of the tensor effect may vary the RPA and the SSRPA results. We adopted two extreme cases in this paper: how the energies and the strengths are affected by the tensor forces. In the present results, we demonstrated that the tense effects are seen even in the natural-parity states in the SSRPA results, while it is negligible in the RPA level except in the case of the 3^- state. Some tensor parameter sets will improve more the descriptions of the transition probabilities of low-lying states. This study remains for the future work.

To study the microscopic structure of the first low-lying excited states, 0_1^+, 2_1^+, and 3_1^-, the norms of 1p-1h and 2p-2h amplitudes are tabulated in Tables II–VII. It was shown that the main 1p-1h configurations of 0_1^+ and 2_1^+ in both ^{16}O and ^{40}Ca are spin-non-flip configurations and the tensor effect is rather small. For the 3_1^- state, on the other hand, the dominant 1p-1h configuration is the spin-flip configuration and the tensor forces have substantial effects on these configurations even in the 1p-1h RPA model space.

Inspired by the present numerical applications of the tensor forces in the SSRPA model, spin-dependent collective excitations such as the magnetic, Gamow-Teller, and charge-exchange spin-dipole transitions are quite interesting subjects to explore and will be studied in the near future.

ACKNOWLEDGMENTS

We are grateful to Di Wu and Dazhuang Chen for fruitful discussions. This work is supported by the National Natural Science Foundation of China under Grants No. 11575120 and No. 11822504, by the Science Specialty Program of Sichuan University under Grant No. 2020SCUNL210, and by JSPS KAKENHI Grant No. JP19K03858.

[1] K. Heyde and J. L. Wood, Rev. Mod. Phys. **83**, 1467 (2011).
[2] M. Harakeh, A. Arends, M. De Voigt, A. Drentje, S. Van der Werf, and A. Van Der Woude, Nucl. Phys. A **265**, 189 (1976).
[3] D. Tilley, H. Weller, and C. Cheves, Nucl. Phys. A **564**, 1 (1993).
[4] Y.-W. Lui, H. L. Clark, and D. H. Youngblood, Phys. Rev. C **64**, 064308 (2001).
[5] M. Ulrickson, N. Benczer-Koller, J. R. MacDonald, and J. W. Tape, Phys. Rev. C **15**, 186 (1977).
[6] D. H. Youngblood, Y.-W. Lui, and H. L. Clark, Phys. Rev. C **55**, 2811 (1997).
[7] D. H. Youngblood, Y.-W. Lui, and H. L. Clark, Phys. Rev. C **63**, 067301 (2001).
[8] T. Kibédi and R. H. Spear, At. Data Nucl. Data Tables **80**, 35 (2002).

[9] T. Hartmann, J. Enders, P. Mohr, K. Vogt, S. Volz, and A. Zilges, Phys. Rev. C **65**, 034301 (2002).
[10] E. Caurier, G. Martínez-Pinedo, F. Nowacki, A. Poves, and A. P. Zuker, Rev. Mod. Phys. **77**, 427 (2005).
[11] E. Caurier, J. Menéndez, F. Nowacki, and A. Poves, Phys. Rev. C **75**, 054317 (2007).
[12] N. Paar, Y. F. Niu, D. Vretenar, and J. Meng, Phys. Rev. Lett. **103**, 032502 (2009).
[13] I. Daoutidis and P. Ring, Phys. Rev. C **83**, 044303 (2011).
[14] M. Martini, S. Péru, and M. Dupuis, Phys. Rev. C **83**, 034309 (2011).
[15] G. Colò, L. Cao, N. Van Giai, and L. Capelli, Comput. Phys. Commun. **184**, 142 (2013).
[16] G. Tertychny, V. Tselyaev, S. Kamerdzhiev, F. Grümmer, S. Krewald, J. Speth, E. Litvinova, and A. Avdeenkov, Nucl. Phys. A **788**, 159 (2007).
[17] N. Lo Iudice and Ch. Stoyanov, Phys. Rev. C **62**, 047302 (2000).
[18] G. Colò, H. Sagawa, and P. F. Bortignon, Phys. Rev. C **82**, 064307 (2010).
[19] Y. F. Niu, G. Colò, M. Brenna, P. F. Bortignon, and J. Meng, Phys. Rev. C **85**, 034314 (2012).
[20] S. Kamerdzhiev, J. Speth, and G. Tertychny, Eur. Phys. J. A **7**, 483 (2000).
[21] G. F. Bertsch and I. Hamamoto, Phys. Rev. C **26**, 1323 (1982).
[22] D. Gambacurta, M. Grasso, and F. Catara, Phys. Rev. C **81**, 054312 (2010).
[23] D. Gambacurta, M. Grasso, and F. Catara, Phys. Rev. C **84**, 034301 (2011).
[24] N. D. Dang and A. Arima, Phys. Rev. Lett. **80**, 4145 (1998).
[25] R. Mohan, M. Danos, and L. C. Biedenharn, Phys. Rev. C **3**, 1740 (1971).
[26] T. Yamada, Y. Funaki, T. Myo, H. Horiuchi, K. Ikeda, G. Röpke, P. Schuck, and A. Tohsaki, Phys. Rev. C **85**, 034315 (2012).
[27] J. Da Providência, Nucl. Phys. **61**, 87 (1965).
[28] C. Yannouleas, Phys. Rev. C **35**, 1159 (1987).
[29] A. Shizuko and Y. Shiro, Nucl. Phys. A **306**, 53 (1978).
[30] B. Schwesinger and J. Wambach, Nucl. Phys. A **426**, 253 (1984).
[31] C. Yannouleas, M. Dworzecka, and J. Griffin, Nucl. Phys. A **397**, 239 (1983).
[32] S. Drozdz, V. Klemt, J. Speth, and J. Wambach, Nucl. Phys. A **451**, 11 (1986).
[33] P. Papakonstantinou and R. Roth, Phys. Lett. B **671**, 356 (2009).
[34] P. Papakonstantinou and R. Roth, Phys. Rev. C **81**, 024317 (2010).
[35] D. Gambacurta and F. Catara, Phys. Rev. B **79**, 085403 (2009).
[36] K. Moghrabi, M. Grasso, G. Colò, and N. Van Giai, Phys. Rev. Lett. **105**, 262501 (2010).
[37] D. J. Thouless, Nucl. Phys. **22**, 78 (1961).
[38] P. Papakonstantinou, Phys. Rev. C **90**, 024305 (2014).
[39] V. I. Tselyaev, Phys. Rev. C **75**, 024306 (2007).
[40] V. I. Tselyaev, Phys. Rev. C **88**, 054301 (2013).
[41] D. Gambacurta, M. Grasso, and J. Engel, Phys. Rev. C **92**, 034303 (2015).
[42] D. Gambacurta, M. Grasso, V. De Donno, G. Cò, and F. Catara, Phys. Rev. C **86**, 021304(R) (2012).
[43] T. Otsuka, T. Suzuki, R. Fujimoto, H. Grawe, and Y. Akaishi, Phys. Rev. Lett. **95**, 232502 (2005); T. Otsuka, T. Matsuo, and D. Abe, *ibid.* **97**, 162501 (2006).
[44] G. Colò, H. Sagawa, S. Fracasso, and P. F. Bortignona, Phys. Lett. B **646**, 227 (2007); **668**, 457 (2008).
[45] D. M. Brink and Fl. Stancu, Phys. Rev. C **75**, 064311 (2007).
[46] B. A. Brown, T. Duguet, T. Otsuka, D. Abe, and T. Suzuki, Phys. Rev. C **74**, 061303(R) (2006).
[47] J. Dobaczewski, in *Proceedings of the Third ANL/MSU/JINA/INT RIA Workshop*, edited by T. Duguet, H. Esbensen, K. M. Nollett, and C. D. Roberts (World Scientific, Singapore, 2006).
[48] T. Lesinski, M. Bender, K. Bennaceur, T. Duguet, and J. Meyer, Phys. Rev. C **76**, 014312 (2007).
[49] M. Grasso, Z. Y. Ma, E. Khan, J. Margueron, and N. Van Giai, Phys. Rev. C **76**, 044319 (2007).
[50] W. Zou, G. Colò, Z. Y. Ma, H. Sagawa, and P. F. Bortignon, Phys. Rev. C **77**, 014314 (2008).
[51] M. Zalewski, J. Dobaczewski, W. Satula, and T. R. Werner, Phys. Rev. C **77**, 024316 (2008).
[52] G. Colò, Bulk nuclear properties, in *Proceedings of the Fifth ANL/MSU/JINA/INT FRIB Workshop*, edited by P. Danielewicz, AIP Conf. Proc. No. 1128 (American Institute of Physics, Melville, NY, 2009), p. 59.
[53] D. Wu, C. L. Bai, H. Sagawa, Z.-Q. Song, and H. Q. Zhang, Nucl. Sci. Tech. **31**, 14 (2020).
[54] Y. Z. Wang, J. Z. Gu, J. M. Dong, and X. Z. Zhang, Phys. Rev. C **83**, 054305 (2011).
[55] J. M. Dong, W. Zuo, J. Z. Gu, Y. Z. Wang, L. G. Cao, and X. Z. Zhang, Phys. Rev. C **84**, 014303 (2011).
[56] A. Li, E. Hiyama, X. R. Zhou, and H. Sagawa, Phys. Rev. C **87**, 014333 (2013).
[57] J. Navarro and A. Polls, Phys. Rev. C **87**, 044329 (2013).
[58] C. L. Bai, H. Sagawa, H. Zhang, X. Zhang, G. Colò, and F. Xu, Phys. Lett. B **675**, 28 (2009).
[59] C. L. Bai, H. Q. Zhang, X. Z. Zhang, F. R. Xu, H. Sagawa, and G. Colò, Phys. Rev. C **79**, 041301(R) (2009).
[60] L.-G. Cao, G. Colò, H. Sagawa, P. F. Bortignon, and L. Sciacchitano, Phys. Rev. C **80**, 064304 (2009).
[61] D. Davesne, M. Martini, K. Bennaceur, and J. Meyer, Phys. Rev. C **80**, 024314 (2009).
[62] L.-G. Cao, G. Colò, and H. Sagawa, Phys. Rev. C **81**, 044302 (2010).
[63] L.-G. Cao, H. Sagawa, and G. Colò, Phys. Rev. C **83**, 034324 (2011).
[64] L. J. Jiang, S. Yang, B. Y. Sun, W. H. Long, and H. Q. Gu, Phys. Rev. C **91**, 034326 (2015).
[65] G. L. Yu, J. Z. Gu, Y. Z. Wang, Z. Y. Li, and G. Q. Meng, Sci. China.: Phys., Mech. Astron. **57**, 1662 (2014).
[66] L. J. Jiang, S. Yang, J. M. Dong, and W. H. Long, Phys. Rev. C **91**, 025802 (2015).
[67] D. Davesne, P. Becker, A. Pastore, and J. Navarro, Phys. Rev. C **93**, 064001 (2016).
[68] Z.-H. Wang, Q. Zhao, H. Z. Liang, and W. H. Long, Phys. Rev. C **98**, 034313 (2018).
[69] S. Wang, H. Tong, P. Zhao, and J. Meng, Phys. Rev. C **100**, 064319 (2019).
[70] J. Geng, J. Xiang, B. Y. Sun, and W. H. Long, Phys. Rev. C **101**, 064302 (2020).
[71] C. L. Bai, H. Q. Zhang, X. Z. Zhang, F. R. Xu, H. Sagawa, and G. Colò, Chin. Phys. Lett. **27**, 102101 (2010).
[72] C. L. Bai, H. Q. Zhang, H. Sagawa, X. Z. Zhang, G. Colò, and F. R. Xu, Phys. Rev. Lett. **105**, 072501 (2010).

[73] M. Anguiano, G. Cò, V. De Donno, and A. M. Lallena, Phys. Rev. C **83**, 064306 (2011).
[74] F. Minato and C. L. Bai, Phys. Rev. Lett. **110**, 122501 (2013).
[75] M. T. Mustonen and J. Engel, Phys. Rev. C **93**, 014304 (2016).
[76] C. L. Bai, H. Q. Zhang, H. Sagawa, X. Z. Zhang, G. Colò, and F. R. Xu, Phys. Rev. C **83**, 054316 (2011).
[77] V. De Donno, G. Cò, M. Anguiano, and A. M. Lallena, Phys. Rev. C **90**, 024326 (2014).
[78] A. A. Dzhioev, A. I. Vdovin, G. Martinez-Pinedo, J. Wambach, and Ch. Stoyanov, Phys. Rev. C **94**, 015805 (2016).
[79] V. De Donno, G. Cò, M. Anguiano, and A. M. Lallena, Phys. Rev. C **93**, 034320 (2016).
[80] I. Deloncle, S. Péru, and M. Martini, Eur. Phys. J. A **53**, 170 (2017).
[81] E. O. Sushenok, A. P. Severyukhin, N. N. Srsenyev. and I. N. Borzov, Acta. Phys. Pol., B **50**, 261 (2019).
[82] B. S. Hu, Q. Wu, Q. Yuan, Y. Z. Ma, X. Q. Yan, and F. R. Xu, Phys. Rev. C **101**, 044309 (2020).
[83] Z. Wang, T. Naito, H. Liang, and W. H. Long, Phys. Rev. C **101**, 064306 (2020).
[84] A. A. Dzhioev, S. V. Sidorov, A. I. Vdovin, and T. Yu. Tretyakova, Phys. At. Nucl. **83**, 143 (2020).
[85] N. Van Giai and H. Sagawa, Phys. Lett. B **106**, 379 (1981).